Research Article
doi.org/10.1002/celc.202101477

Chemistry Europe
European Chemical Societies Publishing

www.chemelectrochem.org

Embedded Double One-Dimensional Composites of WO_3@N-Doped Carbon Nanofibers for Superior and Stabilized Lithium Storage

Jiaxuan Yang,[a] Shenyu Du,[a] Liyuan Ao,[a] Jihao Zhang,[a] Chunqiao Jin,[a] Meijie Han,[a, d] Kai Jiang,[a] Liyan Shang,[a] Yawei Li,[a] Jinzhong Zhang,[a] Liangqing Zhu,[a] Zhigao Hu,*[a, b, c] and Junhao Chu[a, b, c]

Tungsten oxide has received plenty of attention as a potential anode material for lithium-ion batteries (LIBs) due to the high intrinsic density and abundant framework diversity. However, the tremendous structural and volumetric changes of tungsten oxide (WO_3) restrict the commercial application. A novel embedded one-dimensional (1D) structure composite of the WO_3 and N-doped carbon nanofibers (WO_3@N-CNFs) has been prepared by combining convenient hydrothermal and electrospinning processes. The WO_3 nanowires are firmly wrapped in the N-CNFs and formed an embedded double 1D structure, which can significantly improve the structure stability of the composite. Therefore, the WO_3@N-CNFs delivers a high specific capacity of 960 mAh/g after 300 cycles at 0.2 A/g, and 550 mAh/g after 1300 cycles at 2 A/g. Moreover, the initial Coulomb efficiency of WO_3@N-CNFs is enhanced to more than 80%. The electrochemical performance is better than those from most WO_3-based carbon composite materials, which can be ascribed to the synergy effects of the WO_3 nanorods and the nitrogen doping in 1D carbon nanofibers. As a consequence, the WO_3@N-CNFs can be a promising anode material with the extraordinary long-term cycling performance at high current densities, and provide a new idea for the commercialization of WO_3-based carbon composite materials.

Introduction

Lithium-ion batteries (LIBs) have become the mainstay of energy storage devices due to their high energy density, excellent cycling performance, flexible and lightweight design.[1–5] It is precisely because of the above characteristics that LIBs are widely used in many fields, such as hybrid electrical vehicles, grid-scale batteries, new power-intensive devices, smart grid and so on.[6–11] The choice of anode material plays an important role in improving the performance of lithium-ion batteries. The current popular commercial anode material, graphite, has a theoretical capacity of only 372 mAh/g, which cannot meet the demand for high power/energy density.[12] Tungsten oxide (WO_3), as a transition metal oxide, has a theoretical capacity of 693 mAh/g and a large crystal lattice spacing (3.7 Å), making it an ideal choice for anode materials.[13,14] However, the poor conductivity of WO_3 and the huge volume change during the insertion and conversion of lithium ions can easily cause the collapse of the lattice structure, resulting in a rapid decrease in specific capacity. Therefore, further research and exploration should be carried out for the application of WO_3 anode materials for LIBs.

In order to solve these issues, tremendous efforts have been made to improve the conductivity and structural stability of WO_3. In recent years, researchers have been pursuing to reduce the size of WO_3 and synthesize low-dimensional structure to improve the rate and cycle performance of LIBs.[15–17] For instance, Sasidharan *et al.* prepared WO_3 hollow nanospheres of extremely small size with excellent rate performance.[15] Lian *et al.* prepared hexagonal ultrathin WO_3 nano-ribbons as an anode material for high performance.[16] Zhang *et al.* prepared a novel ulthathin $W_{18}O_{49}$@carbon nanowire web, which exhibits good electrochemical performance as an anode material in LIBs.[17] However, the cycle performance of the above works still needs to be improved. Thus, one-dimensional carbon nanofibers are introduced to improve the cycle performance of the batteries. Electrospinning technology has attracted plenty of attention due to its simple structure, strong versatility, great size controllability, and large output. Through electrospinning

[a] J. Yang, Dr. S. Du, Dr. L. Ao, J. Zhang, Dr. C. Jin, Dr. M. Han, Dr. K. Jiang, Dr. L. Shang, Dr. Y. Li, Dr. J. Zhang, Dr. L. Zhu, Prof. Z. Hu, Prof. J. Chu
Technical Center for Multifunctional Magneto-Optical Spectroscopy (Shanghai), Engineering Research Center of Nanophotonics & Advanced Instrument (Ministry of Education), Department of Materials, School of Physics and Electronic Science, East China Normal University, Shanghai 200241, China
Tel.: +86-21-54345150
Fax: +86-21-543452933
E-mail: zghu@ee.ecnu.edu.cn
[b] Prof. Z. Hu, Prof. J. Chu
Collaborative Innovation Center of Extreme Optics, Shanxi University, Taiyuan, Shanxi 030006, China
[c] Prof. Z. Hu, Prof. J. Chu
Shanghai Institute of Intelligent Electronics & Systems, Fudan University, Shanghai 200433, China
[d] Dr. M. Han
School of Electrical Engineering, Shanghai Dianji University, Shanghai 201306, China

Supporting information for this article is available on the WWW under https://doi.org/10.1002/celc.202101477

© 2021 Wiley-VCH GmbH

and subsequent annealing process, the morphology (porous, hollow, core-shell) and the one-dimensional component (metal/metal oxide, carbon/metal or metal composite oxide) of the product can be suitably controlled. It means that the nanofibers produced by electrospinning have a large surface area to volume ratio, which can provide many active sites for the interpenetration of lithium ions. At the same time, its porous structure can effectively buffer the huge volume changes during electrochemistry reaction, and has strong mechanical force to prevent the lattice structure of metal oxide from collapse.[18] As a result, owing to the poor conductivity and the huge volume change of the WO_3 as the anode of LIBs, the one-dimensional carbon nanofibers prepared by electrospinning can effectively improve its cycle performance.

Herein, we demonstrate a method of embedding WO_3 nanowires into one-dimensional carbon nanofibers. In the resulting product, the carbon nanofibers perfectly wrapped the WO_3 nanowires to form embedded WO_3@N-CNFs composite. The WO_3 prepared by the hydrothermal method was evenly dispersed in the electrospinning precursor. In the product obtained, the carbon nanofibers perfectly wrap the WO_3 nanowires to form an embedded structural WO_3@CNFs. Uniform and complete one-dimensional WO_3@N-CNFs composite structure can effectively solve the volume expansion problem caused by the intercalation and conversion of WO_3 and lithium-ions. The one-dimensional channel is also conducive to the N-CNFs, as the transmission of electrons can increase the specific surface area. Therefore, the performance of the lithium-ion batteries using WO_3@CNFs as the anode material has been greatly improved, as compared to pure WO_3 system.

Results and Discussion

As shown in Figure 1, the synthesis process of dual one-dimensional embedded WO_3@N-CNFs is demonstrated. Firstly, the WO_x nanowires were synthesized via a one-step hydrothermal process at 180 °C for 10 h. The electrospinning process was conducted using a precursor solution prepared by dispersing WO_x nanowires and dissolving PAN in DMF. To obtain WO_3@N-CNFs, the collected electrospun WO_x/PAN fibers were first stabilized in air at 250 °C, then the composite was calcined at 700 °C in Ar for carbonization. After annealing, a double one-dimensional composite embedded structure is obtained, which reduces the internal defects of WO_3@N-CNFs. It prevents the direct contact between WO_3 and the electrolyte, meanwhile restrains the volume expansion. The import of carbon nanofibers enhances the crystallinity and stability of the structure.

As shown in Figure 2a, XRD analysis was used to determine the crystal structure of WO_x nanowires synthesized under hydrothermal conditions and WO_3@N-CNF synthesized under annealing conditions. The typical peaks at 23.5° and 37.2° of WO_x nanowires correspond to the (010) and (114) planes of $WO_{2.83}$ (JCPDS# 36-0103). The (010) plane has the highest XRD peak intensity, which indicates that WO_x nanowires grow along the (010) direction.[11] The typical peaks in the range of 22°–24° of WO_3@N-CNFs correspond to the (002), (020) and (200) planes of WO_3 (JCPDS# 32–1395). These results verified the transition from WO_x to WO_3, which are consistent with the subsequent results. The carbon content in the WO_3@N-CNFs samples was tested by the thermogravimetric analysis (TGA). It can be seen from Figure 2b that the carbon content of WO_3@N-CNFs is 51.3 %, the rest is WO_3.

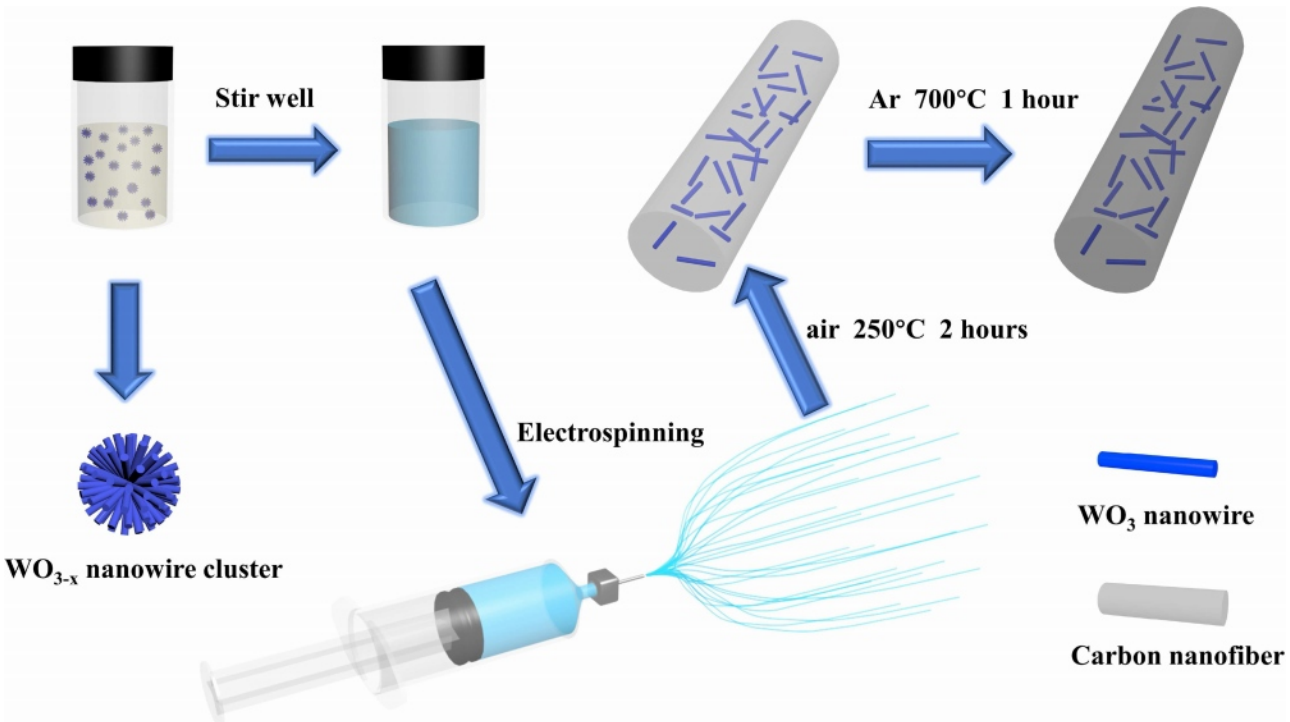

Figure 1. Schematic diagram of preparation of embedded double one-dimensional WO_3@N-CNFs composite structure material.

© 2021 Wiley-VCH GmbH

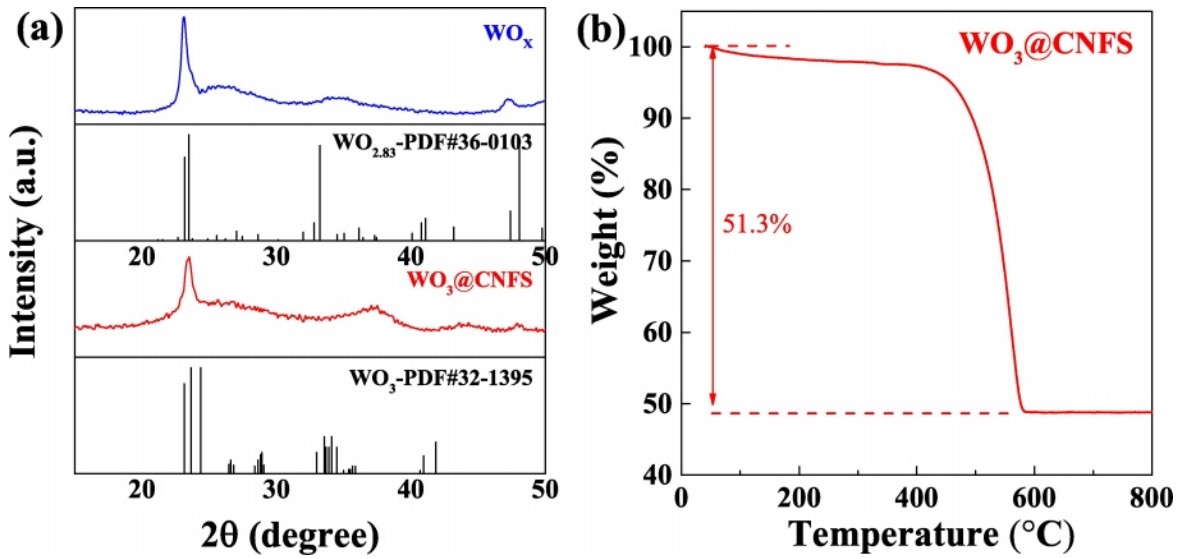

Figure 2. a) XRD patterns of as-prepared WO_x and WO_3@N-CNFs samples and b) thermogravimetric analysis of WO_3@N-CNFs under a heating rate of 10 °C min^{-1}.

It can be seen from Figure 3 (Figure S1, S2), SEM and TEM were used to characterize the morphology and the microstructure of the WO_x nanowires and WO_3@N-CNFs. From Figure 3a,b, it can be seen that the hydrothermally generated WO_x has a nanowire structure with a size of between 20–30 nm. Because its size is too small, it agglomerates into a spherical shape. According to the previous studies, amino groups may be generated in the first pretreatment stage of electrospinning nanofibers with PAN, thereby inhibiting the fusion of nanofibers during the post-carbonization process.[19] As shown in Figure 3c,d, the surface of WO_3@N-CNFs is smooth and the size is uniform, and located between 200–300 nm. The nanowires are completely wrapped by carbon nanofibers, which can effectively inhibit the volume expansion during lithium removal and lithium insertion, and ensure the stability of the cycle during charging and discharging. As shown in Figure 3e,f, the dark black part is WO_3 nanowires, and the light gray part is carbon nanofibers. Obviously, the carbon nanofibers perfectly wrap the WO_3 nanowires.

In order to further reveal the lattice orientation and internal micro/nano structure of WO_3@N-CNFs nanocomposites, HRTEM and EDS characterizations have been performed. As shown in Figure 4a,b (Figure S2), the lattice fringe spacing is close to 0.39 nm, which corresponds to the growth direction along the (002) direction. To further demonstrate the distribution of WO_3@N-CNFs, the STEM images and corresponding EDS elemental mapping results are provided in Figure 4c-h. The distribution of tungsten and oxygen elements perfectly fits the bright white part in front, which indicates that the WO_3 nanowires are perfectly wrapped and covered by carbon nanofibers and sealed in the carbon layer.

X-ray photoelectron spectroscopy (XPS) was prepared to monitor the composition and functional groups of WO_x nanowires and WO_3@N-CNFS composite materials. The overall spectrum of XPS (Figure 5a) proves that there are O, C and W elements in WO_x nanowires, with no signs of impurities. The main peaks at 531.1, 248.1 and 36.1 eV in the survey spectra corresponding to the elemental species of O 1s, C 1s, and W 4f, respectively. The overall spectrum of XPS (Figure 5d) proves that there are O, N, C and W elements in WO_3@N-CNFs composite materials. The main peaks at 531.1, 399.1, 285.1 and 36.1 eV in the survey spectra corresponding to the elemental species of O 1s, N 1s,C 1s, and W 4f, respectively. It can be seen from Figure 5a,d that the WO_3@N-CNFs has N element compared to WO_x. This is due to the introduction of PAN in electrospinning, among which high polymer PAN has a large amount of N element. Similarly, due to the existence of a large amount of C elements in PAN, the peak intensity of the main peak corresponding to the C element of WO_3@N-CNFs is also very high. As shown in Figure 5b, the two broad peaks in high-solution W 4f spectrum of the WO_3 could be fitted into four peaks, corresponding to the W $4f_{5/2}$ and W $4f_{7/2}$ core levels of W^{6+} and W^{5+} cations, respectively. The binding energy peaks observed at 38.1 and 36.0 eV are due to the presence of W^{6+}, while the peaks at 36.7 and 34.8 eV are consistent with the state of W^{5+}. All these prove that there are W^{5+} and W^{6+} characteristic peaks in the spectrum of WO_x nanowires.[20] Figure 5e showed the W 4f spectrum of WO_3@N-CNFs, which could be deconvoluted into two peaks, corresponding to the W $4f_{5/2}$ and W $4f_{7/2}$ core levels, respectively. The binding energy peaks observed at 37.8 and 35.7 eV are due to the presence of W^{6+}. This proves that WO_3@N-CNFs only has W^{6+} state.[12] As shown in Figure 5b,e, it can be concluded that there are only W^{6+} characteristic peaks in the spectrum of WO_3@N-CNFs, while the W^{5+} and W^{6+} characteristic peaks in the spectrum of WO_x. This verifies the conclusion of the XRD pattern. The transition from WO_x to WO_3 increases the O content and provides more active sites for the reaction.[21] It can be seen from Figure 5c, the O 1s spectra could be matched with four peaks at 532.7, 531.7, 530.9 and 530.4 eV, belonging to O=C, W–OH, O=W and O–W bonds

© 2021 Wiley-VCH GmbH

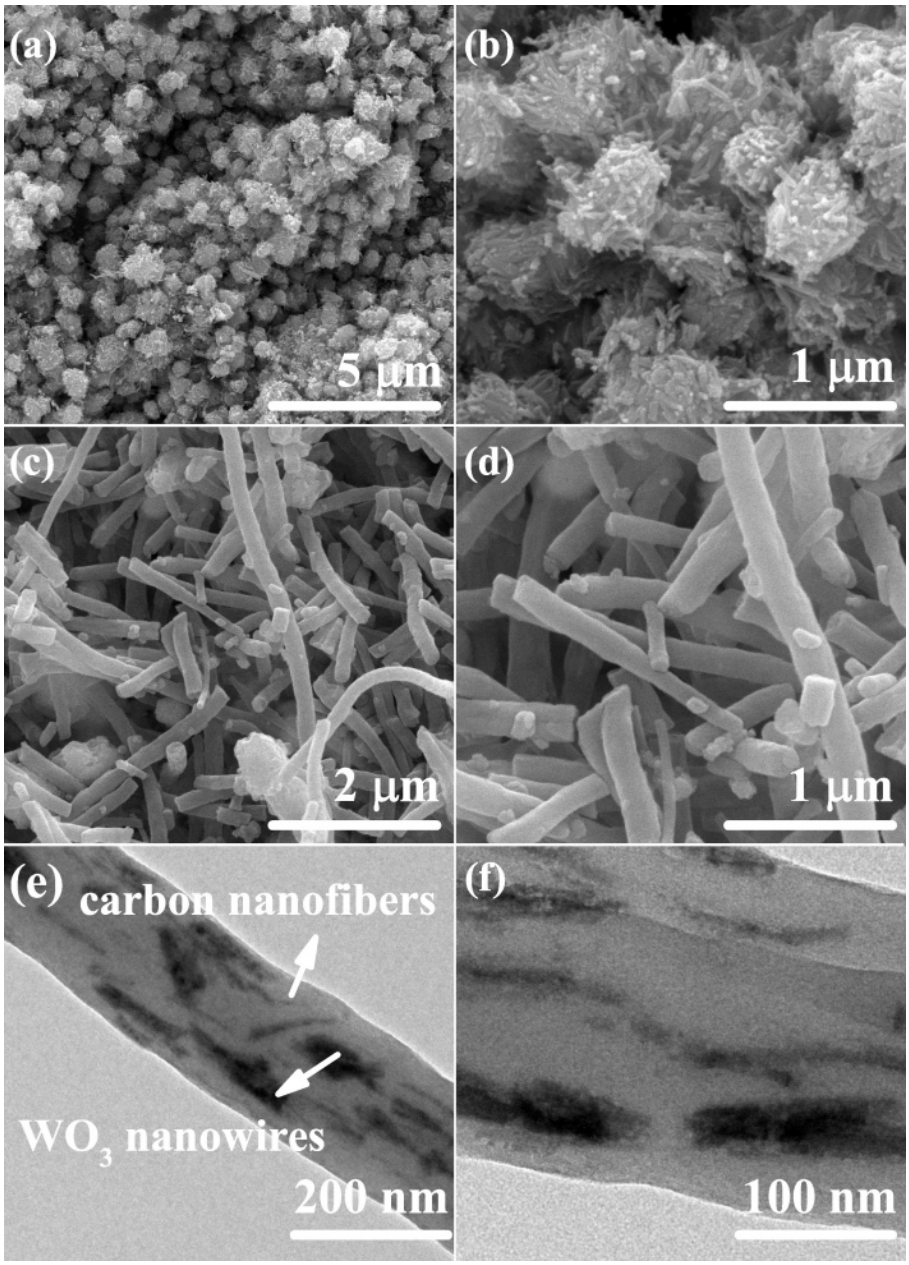

Figure 3. a,b) SEM images of WO_x nanowires. c,d) SEM images of WO_3@N-CNFs. e,f) TEM images of WO_3@N-CNFs.

in several.[22] Similarly, it can be seen from Figure 5f, the O 1s spectra could be matched with three peaks at 532.7, 531.6 and 530.7 eV, belonging to O=C, W-OH and O–W bonds respectively. In contrast, the lack of O=W also confirms the complement of oxygen vacancies in WO_x.

In Figure 6a-d, the cyclic voltammetry (CV) curves of the WO_3@N-CNFs electrode were tested to explore the Lithium ion storage mechanism. As shown in Figure 6a, cyclic voltammetry (CV) was tested to confirm the reversibility of the electrode material, with a scan rate of 0.5 mV/s from 0.01 to 3.0 V (vs. Li^+/Li). The reduction peak at 1.386 V indicates the process of lithium insertion. At the same time, the oxidation peaks at 1.255, 1.899 and 2.603 V reveal the extraction process of lithium. When WO_3 was applied as an anode material, according to the following charge-discharge mechanism: $WO_3 + 6Li^+ + 6e^- \leftrightarrow W + 3Li_2O$.[23] In the first cycle, reduction peak was observed about 0.337 V, corresponding to the formation of a partially irreversible solid electrolyte interphase (SEI) layer.[24] The thermodynamic reaction potential of WO_3 is 1.6 V, which indicates that the overpotential observed at 1.386 V can be ascribed to the kinetic properties of the decomposition of WO_3 to generate metal (W) and Li_2O.[25] The size of WO_3 is smaller than 50 nm, so it can be reasonably inferred that the oxidation peaks at 1.255 and 1.899 V are due to the decomposition of Li_2O and W are oxidized to W^{6+} ions to generate WO_3.[24,25] The oxidation peak of lithium in the WO_3 nanowire electrode was observed at

© 2021 Wiley-VCH GmbH

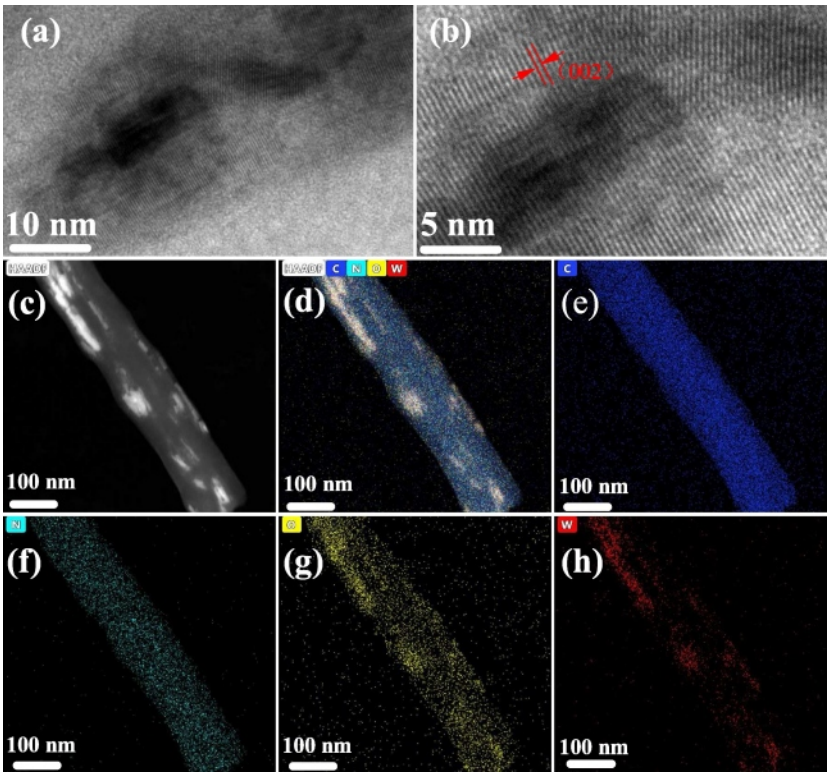

Figure 4. a,b) HRTEM images of WO_3@N-CNFs powders. c,d) STEM images of WO_3@N-CNFs and the relevant elemental mapping images of e) C, f) N, g) O, and h) W.

2.603 V, which can be attributed to the irreversible reaction of impurities from the surface of the nanocrystal. This is consistent with the previous work.[15,26] Compared with the first circle, the second and third circles have no obvious reduction peaks at 0.337 V, which corresponds to the formation of an irreversible SEI layer. Therefore, the morphological characteristics of the CV curve in the subsequent cycles are similar, indicating that the electrochemical reaction in the composite electrode is reversible. Through galvanostatic discharge/charge (GDC) measurement, the electrochemical performance as a negative electrode material for lithium-ion batteries is evaluated. Figure 6b illustrates the charge-discharge curves of WO_3@N-CNFs electrode at a current density of 1 A/g for different cycle numbers. The initial Coulombic efficiency of WO_3@N-CNFs electrode reaches 82.02 %, which is higher than most reports previously used as LIBs anode materials in transition metal oxide materials. This can be ascribed to the perfect combination of WO_3 nanowires and carbon nanofibers. The 50 th, 100 th and 200 th curves overlap completely, which reveals the excellent cycle stability.

As shown in Figure 6c, the CV curves show the similar patterns to further analyze the kinetics mechanism at different rates (0.1-10 mV/s). Considering the high rate performance and rapid lithium ion diffusion, it is believed that the pseudo capacitance can dominate during charge and discharge. The core mechanism between the capacitive contribution and diffusion-controlled contribution can be separated according to the power-law relationship: $i = k_1\nu^{1/2} + k_2\nu = a\nu^b$, where a and b are constants, and n and i are the sweep rate and current, respectively, $k_1\nu^{1/2}$ is the diffusion-controlled contribution and $k_2\nu$ is the capacitive contribution.[27,28] For the diffusion-controlled lithium storage process, the b value is close to 0.5, while for the surface capacitance-based process, the b value is close to 1.0.[29] In order to obtain the b value, the log(ν)-log(i) diagram of the WO_3@N-CNFs electrode is shown in Figure 6d. The values of b are calculated to be 0.84 and 0.99, which confirms that the performance of lithium storage exhibits capacitance-based characteristics, and the charge transfer is rapid. In addition, the capacitance contribution during lithium storage can be inferred by calculating the part of $k_2\nu$. For WO_3@N-CNFs electrode, at a scan rate of 1.0 mV/s, the pseudocapacitive contribution accounts for 91.71% of the entire charge and discharge process (Figure 7a). It can be seen in Figure 7b, the capacitance contribution gradually increases in the histogram when the scan rate increases from 0.2 mV/s to 1.0 mV/s. WO_3@N-CNFs exhibits high ratio of capacitive contribution (75.05%, 80.7%, 84.55%, 88.08%, and 91.71%) at different scan rates from 0.2-1 mV/s. WO_3@N-CNFs has more than 90% capacitive-controlled process at 1 mV/s resulting in high performance. The EIS measurement was used between the new cells and the cells after the rate test for 50 cycles to further discuss the effect of WO_3 on lithium ion diffusion. As shown in Figure 7c, two semicircles can be observed in the Nyquist plots. The first semicircle can be supposed to be the charge transfer resistance (R_{ct}), and the second semicircle can be deemed to the transfer resistance of lithium ion through the SEI film (R_f) which is related to diffusion process of lithium ion.[30] The fitting values

© 2021 Wiley-VCH GmbH

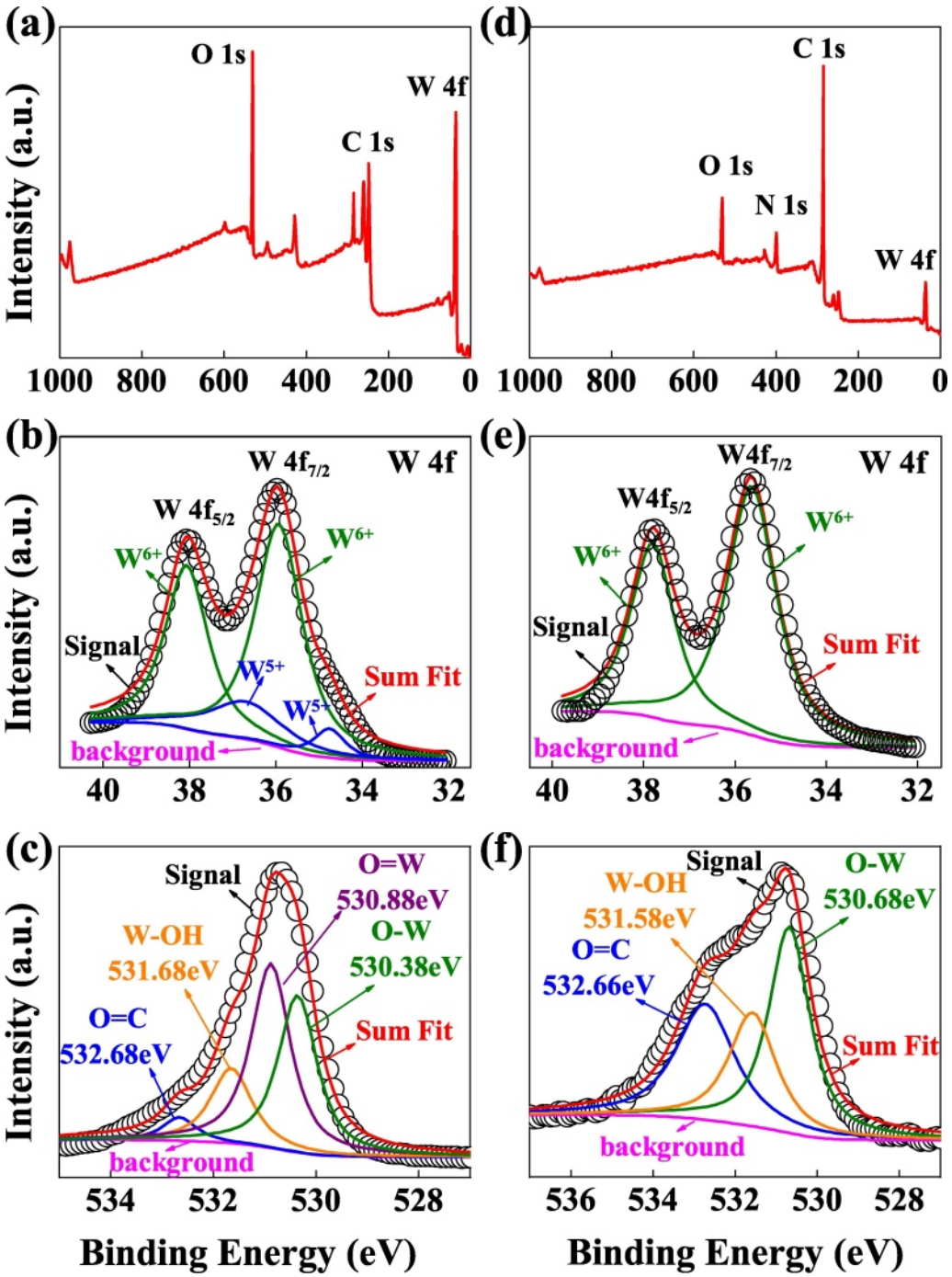

Figure 5. a) XPS spectra of WO_x and high resolution scans of b) W 4f, c) O 1s. d) XPS spectra of WO_3@N-CNFs and high resolution scans of e) W 4f, f) O 1s.

of R_f and R_{ct} are precisely shown in Figure S3, demonstrating that the transfer resistance of Li^+ through the SEI film was increasing continually with the cycling process.

First, the electrochemical performance of WO_x/N-CNF/WO_3@N-CNFs as an anode electrode material for LIBs was tested by galvanostatic charge/discharge (GCD) measurement. The rate capacity and cycle stability of WO_x/N-CNF/WO_3@N-CNFs electrodes were evaluated by the voltage range of 0.01-3 V (vs. Li^+/Li), as shown in Figure 8. Figure 8a shows the rate capacity of WO_x, N-CNF sample and WO_3@N-CNFs electrode at different current densities from 0.1 to 5 A/g and then back to 0.1 A/g, respectively. Compared with the WO_x and N-CNF, the rate performance of WO_3@N-CNFs electrode shows a significant improvement. The WO_3@N-CNFs electrode delivers reversible capacity of 752, 711, 639, 575, 495 and 382 mAh/g from 0.1 to 5 A/g. The specific capacity of WO_3@N-CNFs electrode returns back to 715 mAh/g at 0.1 A/g after 30 cycles. The WO_x electrode delivers reversible capacity of 699, 559, 447, 354, 270 and 189 mAh/g from 0.1 to 5 A/g. The specific capacity of WO_x electrode returns back to 515 mAh/g at 0.1 A/g after 30 cycles. The N-CNF

© 2021 Wiley-VCH GmbH

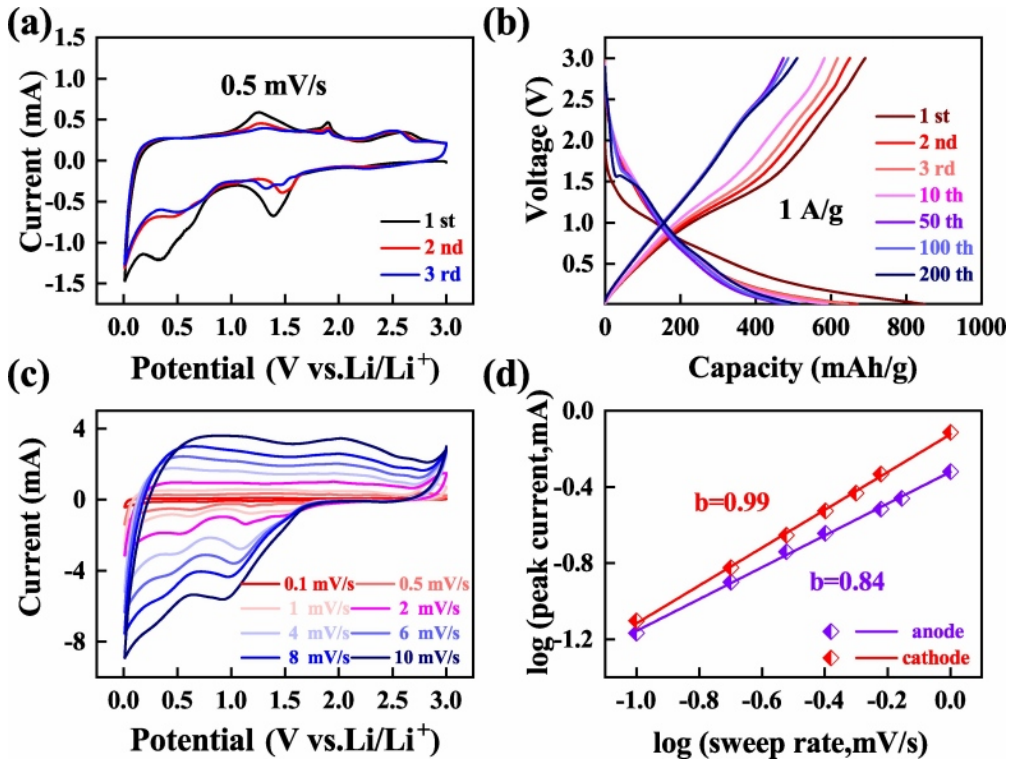

Figure 6. a) CV curves of WO_3@N-CNFs electrode at a scan rate of 0.5 mV/s in the range of 0.01-3.0 V vs. Li/Li^+. b) The GDC profiles of WO_3@N-CNFs for the 1st, 2nd, 3rd, 10th, 50th, 100th, and 200th cycles at 1 A/g. c) CV curves at various rates from 0.1 to 10 mV/s of the WO_3@N-CNFs electrode. d) Graph of the logarithmic peak current and the logarithmic scan rate of the WO_3@N-CNFs electrode.

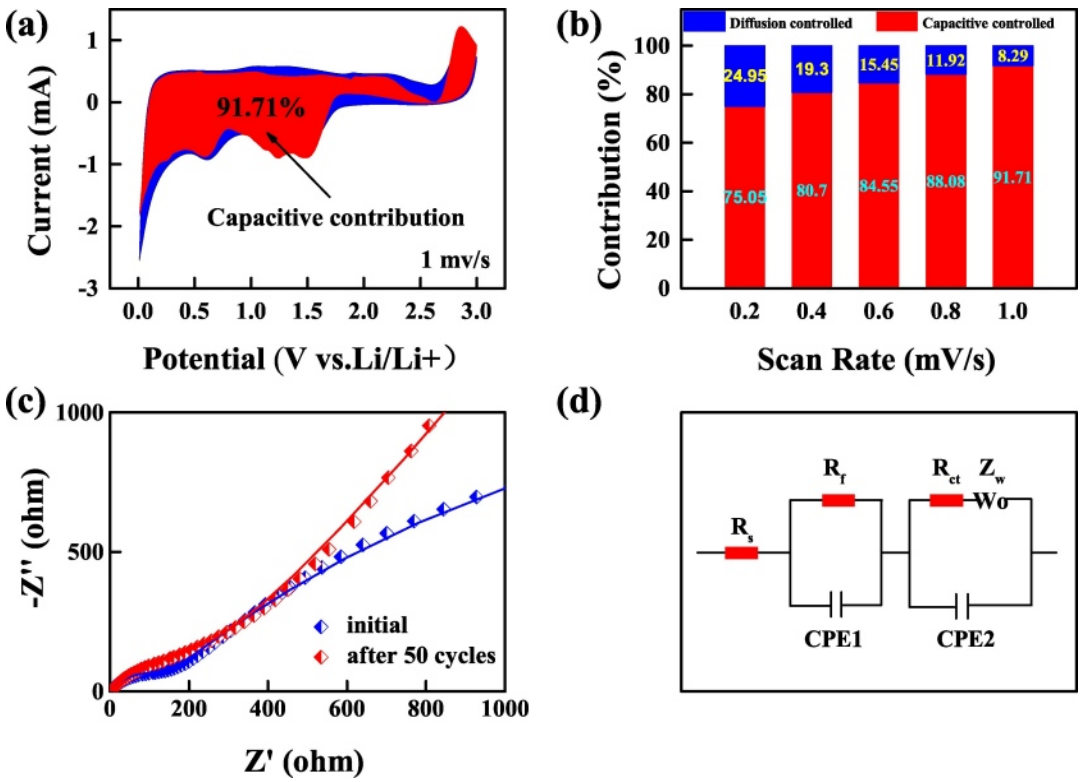

Figure 7. a) Capacitive (red) and diffusion-controlled (blue) contributions of WO_3@N-CNFs at 1 mV/s. b) The contribution of capacitance and diffusion control process at different scan rates of 0.1–10 mV/s. c) Electrochemical impedance spectroscopy of WO_3@N-CNFs electrode at different cycles. d) The equivalent circuit used in EIS.

© 2021 Wiley-VCH GmbH

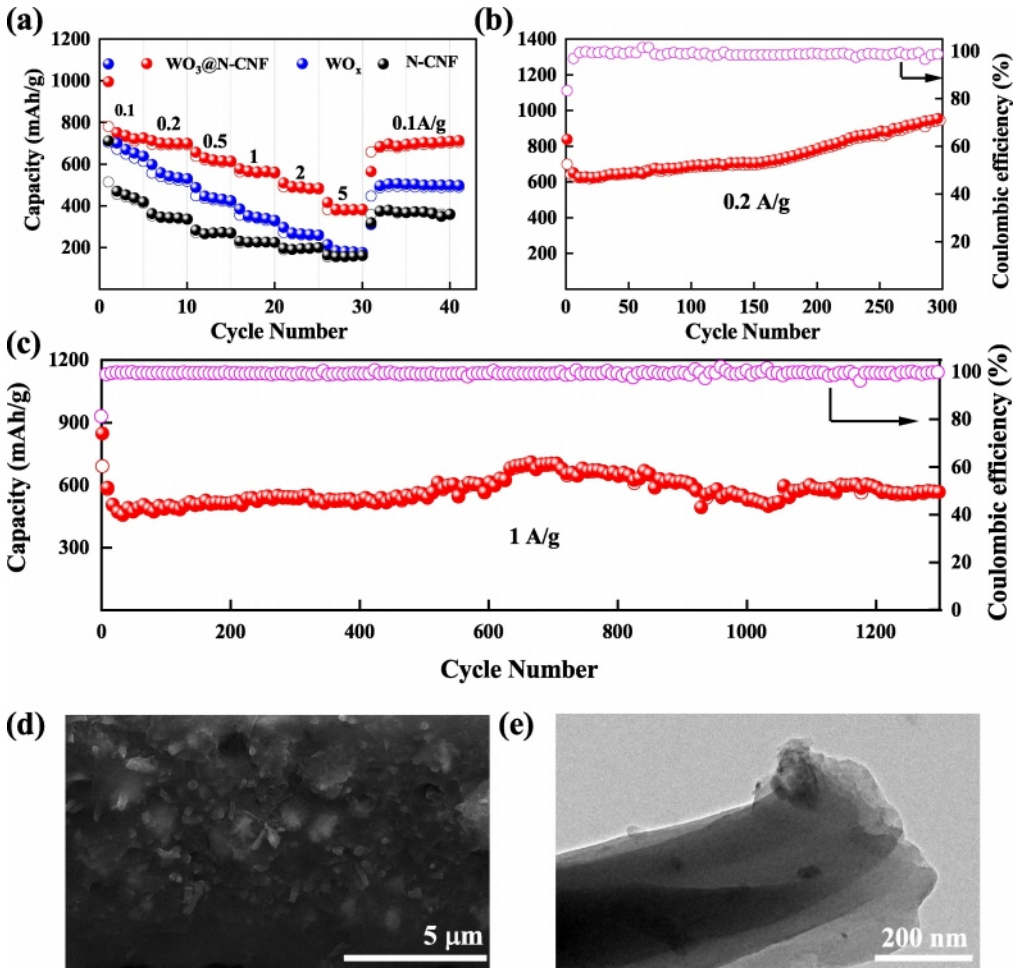

Figure 8. (a) Rate performance of the WO_x/N-CNF/WO_3@N-CNFs electrodes at various current densities. Cycling performance and coulombic efficiency of the WO_3@N-CNFs electrode cycled at (b) 0.2 A/g for 300 cycles and (c) 1 A/g for 1300 cycles. (d)–(e) SEM and TEM images of WO_3@N-CNFs powders after cycling for 300 cycles at 0.2 A/g, respectively.

electrode delivers reversible capacity of 455, 352, 266, 225, 195 and 156 mAh/g from 0.1 to 5 A/g. The specific capacity of N-CNF electrode returns back to 377 mAh/g at 0.1 A/g after 30 cycles. In comparison, the rate performance of WO_3@N-CNFs electrode is fully ahead of WO_x electrode and N-CNF electrode, which fully demonstrates excellent reversibility and stable cycle performance. After comparing the rate performance of the two materials, the importance of carbon coating is highlighted. Without the carbon coating, the WO_3 nanorods will directly contact the electrolyte, causing many side reactions, and even cause the deformation of the WO_3 nanorods and disrupt the lattice structure.[31] As a result, the structure will be unstable during the lithiation/delithiation reaction, resulting in a decrease in capacity, especially at high current densities.

In Figure 8b,c, the stability of WO_3@N-CNFs anode material under different current densities during the charging/discharging process was tested. Figure 8b shows the constant current cycle capability at 0.2 A/g, which lasted for 300 cycles in the voltage range of 0.01-3.0 V (vs. Li^+/Li). The initial discharge capacity was 647 mAh/g at 0.2 A/g. After 170 cycles, the discharge capacity began to increase significantly, and after 300 cycles, the discharge capacity reached 961 mAh/g. The increase of discharge capacity can be attributed to the excellent pseudocapacitance effect and the formation of polymeric gel-like film from degradation of electrolyte.[13] Figure 8d (Figure S5) shows the SEM image of WO_3@N-CNFs powders after cycling for 300 cycles at 0.2 A/g. The SEM images of WO_3@N-CNFs verify the formation of polymeric gel-like film from degradation of electrolyte. The initial coulombic efficiency of WO_3 electrode reaches 83%, and stabilizes above 99% after 15 cycles. Figure 8c shows the constant current cycling capability of 1 A/g, which lasted for 1300 cycles in the voltage range of 0.01-3.0 V (vs. Li^+/Li). At a current density of 1 A/g, the initial discharge capacity is 848 mAh/g. Due to SEI fluctuations and electrolyte decomposition, the WO_3@N-CNFs electrode showed a decrease in capacity during the first 60 cycles.[17] The specific capacity begins to increase,the maximum discharge capacity reaches 710 mAh/g after 660 cycles. Except for the excellent pseudocapacitance effect and the formation of polymeric gel-like film from degradation of electrolyte, the increase in temperature also improves the discharge capacity of the WO_3 electrode. The specific capacity is stabilized at 585 mAh/g after 1300 cycles. As

© 2021 Wiley-VCH GmbH

shown in Figure 8e (Figure S5), the decrease in specific capacity can be ascribed to the agglomeration of WO_3 nanorods. The initial coulombic efficiency of WO_3@N-CNFs electrode reaches 81%, and stabilizes above 99% after 10 cycles. Note that the initial coulombic efficiency is about 70% in the previous work.[32,33] The high initial coulombic efficiency and long cycle stability prove the superiority of WO_3@N-CNFs structure and the potential of transition metal oxides represented by WO_3 as lithium ion anode materials.

Therefore, compared with WO_x, the embedded double one-dimensional WO_3@N-CNFs shows improved electrochemical performance, which is ideal for LIBs with high capacity and long life span. In addition, due to nitrogen doping and carbon sealing, the lithium storage performance of WO_3@N-CNFs electrode exceeds that of most W-based anode materials. The comparison of the cycle performance of WO_3@N-CNFs electrode and W-based anode materials reported in recent years is summarized in Table 1. Therefore, the excellent electrochemical performance can be ascribed to the following causes: (1) the WO_3 nanorods can shorten the diffusion path of Li^+; (2) 1D carbon nanofibers with high mechanical strength can restrict the huge volume change of WO_3 during the Li^+ insertion/extraction process; (3) the formation of polymeric gel-like film from degradation of electrolyte improved the reversible specific capacity of the WO_3@N-CNFs electrode; (4) the nitrogen doping in 1D carbon nanofibers improves the electronic conductivity and provides a large number of lithium ion diffusion channels.

Conclusions

The embedded double one-dimensional WO_3@N-CNFs composite was fabricated by the facile process combining hydrothermal, electrospinning and subsequent annealing. As a consequence, WO_3@N-CNFs exhibited significantly enhanced specific capacity and rate performance as anode of LIBs, because the nano-scale double 1D embedded structure can shorten the diffusion path of Li^+. In addition, the WO_3 nanowires were encapsulated within the N-CNFs, while the nitrogen doping improved the conductivity. Hence, it can accommodate the huge volume change during lithium ion insertion and thereby deliver excellent cycle performance. The design of the structure in this work provide a new strategy to prepare long-life and high-capacity anode materials.

Experimental Section

Material Preparation

WO_3@N-CNFs were prepared by hydrothermal, electrospinning and subsequent annealing process. WO_{3-x} nanowires were prepared by a hydrothermal method. Typically, 333.5 mg of WCl_6 was dissolved into 60 ml ethanol after stirring for 10 minutes. And then the solution was put into a 100 mL Teflon-lined stainless steel autoclave and hydrothermally treated at 180 °C for 10 hours. The blue product obtained is WO_{3-x} nanowires, which were then washed several times with deionized water and ethanol by centrifugation. The product was then placed in a vacuum drying oven at 80 °C overnight. The composite of WO_3 nanowires and carbon nanofibers was prepared by electrospinning. Firstly, 300 mg WO_{3-x} was added to 6 ml of DMF (N,N-Dimethylformamide), and the mixture is evenly stirred. Subsequently, 400 mg of polyacrylonitrile (PAN) was added and stirred at 70 °C. In order to obtain the nanofiber composite structure, the above-mentioned electrospinning precursor solution was transferred to a 5 ml plastic syringe. A 21-gauge injection needle was used for electrospinning at a flow rate of 0.6 mL/h under a high pressure of 15 kV. The obtained fibers were collected with an aluminum foil, which was 13 cm away from the needle-point. Whereafter, the mats with as-electrospun white nanofibers on aluminum foil were dried in vacuum at 80 °C over night. After being completely dried, the mats were taken out and cooled to room temperature. Then they were stabilized at 250 °C for 2 hours in the air, and then carbonized at 700 °C for 1 hour in Ar atmosphere with a heating rate of 2 °C/min.

Material Characterization

In the scanning range of 10° to 60°, the crystal structure of the products was determined by X-ray diffraction (XRD) with Cu-K_α radiation ($\lambda = 1.5418$ Å). Thermogravimetric analysis (TGA) was conducted from 25 to 800 °C in an air atmosphere. The morphology of the samples was characterized by scanning electron microscopy (SEM, PHILIPS XL30TMP), transmission electron microscopy (TEM, TALOS F200X) and the high resolution transmission electron microscopy (HRTEM, TALOS F200X). The surface component of the products was characterized by X-ray photoelectron spectroscopy (XPS, Perkin-Elmer).

Table 1. The cycling performance comparison of the WO_3@N-CNFs electrode and previously reported W-based anode materials.

W-based materials	Current density [A/g]	Capacity [mAh/g]	Cycles [times]	Year	Ref.
N-WO_{3-x}	0.1	954	150	2019	[13]
h-WO_3 hollow nanospheres	0.2 C	332	50	2012	[15]
$W_{18}O_{49}$@carbon nanowire	0.2	889	250	2015	[17]
WO_{3-x} nanosheets	0.1	628	100	2019	[20]
WO_3/RGO	0.15	487	100	2015	[25]
WO_3 nanorods	0.05 C	253	200	2019	[34]
WO_3 nanowires	0.1 C	552	100	2018	[35]
WO_3 thin film	0.2 mA/cm^2	626	60	2010	[36]
h-WO_3 nanotube bundles	0.1	871.9	200	2017	[37]
WO_3 nanorods@N-doped graphene	0.08	828	100	2016	[38]
WO_3@N-CNFs	**0.2**	**961**	**300**		**This work**
	1	**585**	**1300**		

© 2021 Wiley-VCH GmbH

Electrochemical Characterization

The coin-type 2025 cells were used to test the electrochemical performance. The electrodes were manufactured by the traditional slurry-based method in an Ar-filled glovebox. Active materials, acetylene black and polyvinylidene fluoride (PVDF) binder are intensive mixed in the N-methyl-2-pyrrolidone (NMP) at a ratio of 8:1:1. The mass loading of active material in electrode was about 0.78–0.99 mg/cm^2. The homogeneous slurry was pasted onto a clean copper foil and dried at 80 °C overnight in a vacuum oven. The coin-cells were assembled with metallic lithium as counter electrode and celgard 2400 polypropylene film as separator. The galvanostatic discharge-charge (GDC) measurements were carried out on a Land CT 2001A battery tester in a voltage window of 0.01-3 V (vs. Li/Li$^+$). Cyclic voltammetry (CV) test and electrochemical impedance spectroscopy (EIS) was examined using a CHI-660E electrochemical workstation.

Acknowledgements

This work was financially supported by the National Key R&D Program of China (Grant No. 2019YFB2203403), the National Natural Science Foundation of China (Grant Nos. 61974043, 62090013, 61974044, 62074058 and 91833303), the Projects of Science and Technology Commission of Shanghai Municipality (Grant Nos. 21JC1402100 and 19511120100), the Program for Professor of Special Appointment (Eastern Scholar) at Shanghai Institutions of Higher Learning and Shanghai Pujiang Program (20PJ1403600).

Conflict of Interest

The authors declare no conflict of interest.

Data Availability Statement

The data that support the findings of this study are available from the corresponding author upon reasonable request.

Keywords: N-doped carbon nanofibers · electrospinning · pseudocapacitance behavior · lithium-ion batteries · tungsten trioxide

[1] M. B. Zheng, H. Tang, Q. Hu, S. S. Zheng, L. L. Li, J. Xu, H. Pang, *Adv. Funct. Mater.* **2018**, *28*, 1707500.
[2] J. H. Li, H. T. Yan, W. Wei, X. F. Li, L. J. Meng, *ChemElectroChem* **2018**, *5*, 3222–3228.
[3] Y. J. Wu, Y. A. Chen, C. L. Huang, J. T. Su, C. T. Hsieh, S. Y. Lu, *Chem. Eng. J.* **2020**, *400*, 125958.
[4] Q. F. Fu, X. Z. Zhu, R. J. Li, G. S. Liang, L. J. Luo, Y. J. Chen, Y. L. Ding, C. F. Lin, K. K. Wang, X. S. Zhao, *Energy Storage Mater.* **2020**, *30*, 24058297.
[5] L. T. Yang, G. S. Liang, H. G. Cao, S. Y. Ma, X. H. Liu, X. Li, G. Y. Chen, W. B. You, C. F. Lin, R. C. Che, *Adv. Funct. Mater.* **2021**, 2105026.
[6] X. Z. Zhu, J. Xu, Y. P. Luo, Q. F. Fu, G. S. Liang, L. J. Luo, Y. J. Chen, C. F. Lin, X. S. Zhao, *J. Mater. Chem. A* **2019**, *7*, 2050–7488.
[7] K. J. Griffi, K. M. Wiaderek, G. Cibin, L. E. Marbella, C. P. Grey, *Nature* **2018**, *559*, 556.
[8] S. S. Niu, Z. Y. Wang, T. Zhou, M. L. Yu, M. Z. Yu, J. S. Qiu, *Adv. Funct. Mater.* **2017**, *27*, 1605332.
[9] Z. P. Xiao, L. Z. Sheng, L. L. Jiang, Y. Y. Zhao, M. H. Jiang, X. Zhang, M. Y. Zhang, J. Y. Shi, Y. Q. Lin, Z. J. Fan, *Chem. Eng. J.* **2021**, *408*, 127269.
[10] Y. C. Mao, X. D. Zhu, X. H. Fan, H. G. Wang, Z. T. Xu, S. R. Le, *ChemElectroChem* **2019**, *6*, 4560–4564.
[11] C. X. Liu, C. Wang, X. W. Meng, X. Y. Li, Q. Qing, X. N. Wang, R. Y. Xue, Q. Yu, J. L. Yang, K. K. Wang, X. J. Zhao, W. Chen, Z. A. Qiao, X. S. Zhao, *Chem. Eng. J.* **2020**, *339*, 125705.
[12] Z. Q. Zhu, S. W. Wang, J. Du, Q. Jin, T. R. Zhang, F. Y. Cheng, J. Chen, *Nano Lett.* **2014**, *14*, 153–157.
[13] Y. L. S. Cui, K. F. Xiao, N. M. Bedford, X. X. Lu, J. Yun, R. Amal, D. W. Wang, *Adv. Energy Mater.* **2019**, *9*, 1902148.
[14] H. G. Choi, Y. H. Jung, D. K. Kim, *J. Am. Ceram. Soc.* **2005**, *88*, 1684–1686.
[15] M. Sasidharan, N. Gunawardhana, M. Yoshio, K. Nakashima, *Nano Energy* **2012**, *1*, 503.
[16] C. Lian, X. L. Xiao, Z. Chen, Y. X. Liu, E. Y. Zhao, D. S. Wang, C. Chen, Y. D. Li, *Nano Res.* **2016**, *9*, 435–441.
[17] W. H. Zhang, L. Yue, F. Zhang, Q. F. Zhang, X. C. Gui, R. F. Guan, G. H. Hou, N. Xu, *J. Mater. Chem. A* **2015**, *3*, 6102–6109.
[18] J. W. Jung, C. L. Lee, S. Yu, I. D. Kim, *J. Mater. Chem. A* **2016**, *4*, 703–750.
[19] C. Wu, X. H. Zeng, P. He, L. B. Chen, W. F. Wei, *Adv. Mater. Interfaces* 2017, 5, 1701080.
[20] Y. H. Li, K. Chang, H. W. Tang, B. Li, Y. L. Qin, Y. Hou, Z. R. Chang, *Electrochim. Acta* **2019**, *298*, 640–649.
[21] A. I. Inamdar, H. S. Chavan, A. T. A. Ahmed, S. Cho, J. Kim, Y. Jo, S. M. Pawar, Y. Park, H. Kim, H. Im, *Mater. Lett.* **2018**, *215*, 233–237.
[22] Y. Wang, X. Wang, Y. Xu, T. Chen, M. Liu, F. Niu, S. Wei, J. Liu, *Small* **2017**, *13*, 1603689.
[23] S. Yoon, C. Jo, S. Y. Noh, C. W. Lee, J. H. Song, J. Lee, *Phys. Chem. Chem. Phys.* **2011**, *13*, 11060–11066.
[24] S. K. Park, H. J. Lee, M. H. Lee, H. S. Park, *Chem. Eng. J.* **2015**, *281*, 724–729.
[25] D. M. Kim, S. J. Kim, Y. W. Lee, D. H. Kwak, H. C. Park, M. C. Kim, B. M. Hwang, S. Lee, J. H. Choi, S. Hong, K. W. Park, *Electrochim. Acta* **2015**, *163*, 132–139.
[26] Z. J. Gua, H. Q. Lic, T. Y. Zhai, W. S. Yang, Y. Y. Xia, Y. Ma, J. N. Yao, *J. Solid State Chem.* **2007**, *180*, 98–105.
[27] M. L. Li, Q. L. Deng, J. Y. Wang, K. Jiang, Z. G. Hu, J. H. Chu, *Nanoscale* **2018**, *10*, 1–11.
[28] L. Y. Ao, C. Wu, Y. N. Xu, X. Wang, K. Jiang, L. Y. Shang, Y. W. Li, J. Z. Zhang, Z. G. Hu, J. H. Chu, *J. Alloys Compd.* **2020**, *819*, 153036.
[29] J. Y. Wang, C. Wu, Q. L. Deng, K. Jiang, L. Y. Shang, Z. G. Hu, J. H. Chu, *Nanoscale* **2018**, *10*, 13140–13148.
[30] L. Y. Ao, C. Wu, X. Wang, Y. N. Xu, K. Jiang, L. Y. Shang, Y. W. Li, J. Z. Zhang, Z. G. Hu, J. H. Chu, *ACS Appl. Mater. Interfaces* 2**020**, 12, 20824–20837.
[31] S. A. Pervez, D. Kim, F. Zhang, C. H. Doh, U. Farooq, H. Y. Choi, J. H. Choi, *ACS Appl. Mater. Interfaces* **2015**, *7*, 7635–43.
[32] J. F. Yin, H. Q. Cao, J. X. Zhang, M. Z. Qu, Z. F. Zhou, *Cryst. Growth Des.* **2013**, *13*, 759–769.
[33] J. Lee, C. Jo, B. Park, W. Hwang, H. I. Lee, S. Yoon, J. Lee, *Nanoscale* **2014**, *6*, 10147–55.
[34] T. Herdt, D. Deckenbach, M. Bruns, J. J. Schneider, *Nanoscale* **2019**, *11*, 598–610.
[35] Y. R. Lim, Y. Ko, J. Park, W. I. Cho, S. A. Lim, E. Cha, *J. Electrochem. Sci. Technol.* **2019**, *10*, 89–97.
[36] W. J. Li, Z. W. Fu, *Appl. Surf. Sci.* **2010**, *256*, 2447–2452.
[37] X. Wu, S. Yao, *Nano Energy* **2017**, *42*, 143.
[38] X. Gu, F. Wu, B. Lei, J. Wang, Z. Chen, K. Xie, Y. Song, D. Sun, L. Sun, H. Zhou, F. Fang, *J. Power Sources* **2016**, *320*, 231.

Manuscript received: November 7, 2021
Revised manuscript received: December 18, 2021
Accepted manuscript online: December 21, 2021

© 2021 Wiley-VCH GmbH